

Infrared Spectroscopy of Nearby Radio Active Early-Type Galaxies - II: Spectral Atlas

Mark Durré,¹★ Jeremy Mould,¹ Michael Brown² and Tristan Reynolds^{3,4}

¹Centre for Astrophysics & Supercomputing, Swinburne University, Hawthorn VIC 3122, Australia

²School of Physics, Monash University, Clayton, Vic 3800, Australia

³International Centre for Radio Astronomy Research (ICRAR), The University of Western Australia, 35 Stirling Highway, Crawley, WA 6009, Australia

⁴ARC Centre of Excellence for All Sky Astrophysics in 3 Dimensions (ASTRO 3D), Australia

Accepted XXX. Received YYY; in original form ZZZ

ABSTRACT

We present a near infrared spectroscopic atlas of nearby, bright early-type galaxies with radio emission, containing 163 galaxies observed by the Palomar 200'' TripleSpec instrument, measuring the emission line fluxes for H, He, [Fe II] and H₂ and determined the nuclear excitation mechanisms. By stacking spectra, we deduced the H₂ excitation temperature (1957 ± 182 K) and dominant excitation mechanism (thermal and shock heating combined) from the K-band emission line sequence. Stacking also produces an “average” spectrum of absorption features and spectral indices from the literature; the CO12 absorption line index vs. $J - K$ colour shows a trend of stronger nuclear activity producing a weaker CO12 index and a redder (flatter) continuum. The correlations between the radio and the emission-line luminosities finds a trend with radio power; however, the large scatter in the upper limits shows that the two are not directly coupled and the duty cycles of SF and AGN activity are not synchronised.

Key words: galaxies: elliptical and lenticular, cD – galaxies: nuclei – infrared: general – radio continuum: galaxies

1 INTRODUCTION

Early-type galaxies (ETGs) have several advantages for spectroscopic studies of nuclear activity; their fuelling and stellar population is likely to be the simplest, their stored gas is smaller, there is a minimum of nuclear obscuration and nuclear outflows and jets have less ISM to interact with. Near infrared (NIR) observations allow for dust penetration, getting “closer” to the central source (Kennicutt et al. 2009; Brown et al. 2011; Mould et al. 2012; Ricci et al. 2022).

It is highly likely that all massive early-type galaxies ($M_K < -25.5$) are radio continuum sources, presumably harbouring active galactic nuclei (AGN) or undergoing star formation (Brown et al. 2011, hereafter B11). B11 provided an homogeneous sample of 396 bright early-type galaxies ($m_K < 9$, T type < -1 , i.e. Hubble types E and S0), with radio continuum measurements from the NRAO Very Large Array Sky Survey, Green Bank 300 ft Telescope, and 64 m Parkes Radio Telescope; this catalog is well-suited to spectroscopic and multi-wavelength follow-up. This work republishes the complete early-type radio galaxy catalog from B11, supplemented with S0/a galaxies and objects that were observed as described in this paper.

Sabater et al. (2019) cross-compared the LOFAR Two-Metre

Sky Survey (LoTSS) with the Sloan Digital Sky Survey (SDSS) DR7 main galaxy spectroscopic sample, finding the fraction of radio AGN reached 100% at $>10^{11} M_\odot$. Capetti et al. (2022), from their catalog of 188 giant ETGs ($M_K \leq -25$) in their LOFAR sample, obtained 44 SDSS spectra and classified them using Kewley et al. (2006) diagnostics. Of these, the optical spectrum diagnostics showed 11 were AGN (all LINERs) and 7 were star forming (SF); the SF galaxies had a star formation rate (SFR) in the range 0.1–8 $M_\odot \text{ yr}^{-1}$. The rest (26 galaxies) did not have all the diagnostic emission lines detected with enough confidence to be placed on excitation diagrams.

Mould et al. (2012) (hereafter M12) published the results of near-infrared long-slit spectroscopic observations of 136 galaxies from the B11 sample. These were observed in 5 sessions; on the Hale 5m Palomar TripleSpec spectrograph (Herter et al. 2008) (3 sessions) and on the Mayall 4m KPNO Flamingos spectrograph (2 sessions). Of these 20% showed nuclear infrared emission lines, mostly Paschen β and Brackett γ hydrogen lines and [Fe II] lines. Subsequently, further observing sessions using TripleSpec extended the number of objects observed by 96. This work presents the results from the complete observation program and makes the spectra available online.

These observations enable examination of the following science:

- (i) The gaseous excitation mechanism (AGN, star formation or

★ E-mail: mdurre@swin.edu.au

high line ratio- HLR), determined by the emission line flux ratios of H, [Fe II] and H₂.

- (ii) The SFR in the nuclear region (if the object is not an AGN).
- (iii) The warm molecular hydrogen temperature and excitation mechanisms; the H₂ luminosity also estimates the total molecular mass in the nuclear region.
- (iv) Correlations between radio and NIR emissions to examine AGN duty cycles in feeding/feedback models.
- (v) Absorption line studies to determine stellar populations, especially thermally pulsing asymptotic giant branches (TP-AGB) stars which should dominate in younger populations (Martins et al. 2013).

In this work, we determine redshift-dependent distances using the Λ CDM cosmology with parameters $H_0 = 70 \text{ km s}^{-1} \text{ Mpc}^{-1}$, $\Omega_m = 0.3$ and $\Omega_\Lambda = 0.7$.

2 OBSERVATIONS AND DATA REDUCTION

2.1 Observations

The B11 catalog was extended in a follow-up survey to galaxies with morphological T types ≥ 0 (i.e. Hubble types S0/a and S), increasing the total to 514 objects. This extended list was used as the basis for the M12 observations. This was supplemented by inclusion of objects that were observed using TripleSpec as targets of opportunity, but were not included in the previous lists. In total, there are 546 objects in the complete catalog (396 in B11, 118 in the extended survey and 32 TripleSpec supplementary objects). We publish the complete radio survey in this work (see Section 4 below).

Eight observing runs were conducted with the Triplespec instrument subsequent to the data published in M12, making a total of 11 runs. A complete list of these runs are detailed in Table 1, under programs P16, P22, P23 and P220. For each night, we list the number of objects observed that are from the original B11 catalog (Set 1 - 88 galaxies), the extended catalog (Set 2 - 43 galaxies) and the supplementary objects (Set 3 - 32 galaxies), a total of 163 galaxies. Table 2 lists the observational data, showing the galaxy name and observational details. This table is a sample; the complete list is available online, as described below. The detailed attributes for each galaxy may be found in Table 7.

In general, the galaxies were observed in cycles in the standard ABBA mode, separated by 20'' in position on the slit. Each exposure was 300 s, for a total of 1200 s. 20 galaxies were observed with more than one cycle; these are listed in the table where, for example, 1.5 cycles is an observation of ABBAAB positions. The slit aperture was 1'', and the slit was oriented in the east-west direction on the sky.

As noted in M12, the Flamingos observations produced poor results, due to lack of a good data reduction pipeline and instrument flexure. The instrument also does not cover the K-band. However, it was useful for confirming the presence of emission lines (e.g. Pa β and [Fe II]). These observations are not presented in this work.

2.2 Data Reduction

The data reduction was carried out as described in M12, using the SpexTool v4.0 software (Cushing et al. 2004). The software pipeline creates normalized flats and wavelength calibrations (from OH telluric lines) for each night, then for each A–B pair applies flat field correction, traces object spectra, defines extraction apertures,

Table 1. Observation runs with the Hale 5m Palomar TripleSpec spectrograph.

Date (UT)	Run ID	Set 1	Set 2	Set 3	Total
2011-09-15	1	17	1	0	18
2011-09-16	2	22	0	0	22
2012-01-03	3	15	0	0	15
2012-05-28	4	5	0	0	5
2012-05-31	5	7	0	0	7
2013-02-25	6	18	2	2	22
2013-07-31	7	0	0	15	15
2013-08-17	8	0	0	15	15
2013-12-14	9	0	14	0	14
2014-02-14	10	2	13	0	15
2014-02-15	11	2	13	0	15
Totals		88	43	32	163

does background subtracting and extracts and wavelength calibrates spectra. As standard, the spectra are extracted in a window 1''.5 either side of the centre-line (i.e. 3'' total width), and the background starts 3'' from the centre-line. It then combines individual extracted (multi-order) spectra and performs telluric correction and flux calibration, using a standard A0 star which is matched to the spectrum of Vega. It then merges the orders into a single spectrum.

In post-processing on the output of SpexTool, we re-dispersed the original (non-linear) spectrum to a linear wavelength scale (1000–2440 nm) at 0.2 nm resolution (the average over the wavelength range). The TripleSpec instrument has a documented wavelength resolution $\Delta\lambda/\lambda = 2600$, which is equivalent to about 0.65 nm in the middle of the spectral range (~ 943 – 2465 nm). The spectra are cleaned by removing the wavelength ranges 1115–1150 nm, 1330–1480 nm and 1800–1950 nm; these are the atmospheric absorption bands between the Z, J, H and K windows.

The spectra were then inspected and manually cleaned of noise spikes and increased noise near the absorption bands - this was more prominent on spectra with low flux. For a few spectra, the whole was manually cleaned, especially for those that had spectral features near the atmospheric windows (e.g. the He I 1083 nm line of NGC 5548, which would otherwise lose the line wing in the gap). The spectra were then wavelength shifted to restframe. On inspection, almost half the spectra required removal of residual hydrogen line features; these were at zero redshift, caused by imperfect matching of the standard star to the Vega A0 model. These were removed by fitting single (or in a few cases double) Gaussian curves, using the method as described in Section 3.2.

The wavelength calibration can be checked using the Na I doublet at 2206.2/2209.0 nm and the CO bandhead at 2295 nm. Emission lines may be wavelength shifted from radial and/or rotational gas kinematics.

The signal to noise, as given in Table 2, is derived using the DER_SNR algorithm from the Space Telescope Science Institute (STScI)¹. Example plots of the resultant spectra can be seen in M12 (their Figures 1, 2 and 4) and in Figure 1; this shows a variety of nuclear excitation types, star-forming (strong narrow hydrogen lines relative to other emission lines), Seyfert 1 (broad permitted lines of hydrogen and He I) and 2 (narrow permitted lines of similar strength to forbidden lines), HLR (hydrogen lines much weaker than [Fe II] and H₂), and purely absorption (i.e. no activity/emission lines). Figure 1 also labels the major emission lines; the purely absorp-

¹ www.stecf.org/software/ASTROsoft/DER_SNR/

Table 2. Sample object and observation details. (The full table is available online). See Table 7 for the complete properties of each object.

Object	RA	Dec	Cycles	Airmass	Run ID	Standard Star	S/N
2MASX J16251687-0910524	246.3204	-9.1811	1	1.415	8	HD 210290	149.5
IC 0630	159.6401	-7.1707	1	1.344	3	HD 77281	244.0
Mrk 612	52.6703	-3.1377	1	1.425	6	HD 21019	88.8
NGC 0016	2.2678	27.7294	1	1.15	2	HD 221	195.5
NGC 1779	76.3251	-9.1472	1	1.355	11	HD 37887	225.6
NGC 2110	88.0474	-7.4563	1	1.735	2	HD 39439	188.8
NGC 2128	91.1426	57.6277	1	1.366	1	HD 41654	174.6
UGC 3024	65.6108	27.2979	1	1.211	6	HD 283593	130.9
UGC 3426	93.9012	71.0375	1	1.631	1	HD 42507	230.5

tion line sample (NGC 1453) labels the major absorption features; the molecular CO bandheads in the H and K bands, the “bump” in the range ~ 1500 - 1750 nm from the minimum in the opacity of H^- in cool stars (Mason et al. 2015; Rayner et al. 2009) as well as many other absorption lines in the K -band, including the prominent Mg I/CO line at 1711 nm. These absorption and emission lines are discussed in more detail in Section 3.1 and 3.2.

2.3 Sample Characteristics

Figure 2 presents histograms of distributions of redshift (z), morphological type (both of observed vs. all objects, and original vs. extended/supplementary catalogs), K -band absolute magnitude (M_K), luminosity distance, radio power (both including and excluding upper limits) and estimated black-hole mass. The distributions of the observed objects are compared with the full catalog of 546 objects. In general, these match reasonably well, with a bias towards more objects of morphological type 0 (S0/a galaxies) observed than in the complete catalog. By selection, the original vs. extended/supplementary catalogs are ETGs (with no morphological types later than S0) vs. later type galaxies. We also observed objects that have a slightly greater M_K luminosity (and thus computed black hole mass) and radio power. When we exclude upper limits to the radio power, then the two sets are approximately the same. For more details on how these parameters were obtained, see Section 4.

3 RESULTS AND DISCUSSION

3.1 Absorption Features

NIR spectral absorption features can complement optical studies of stellar populations of galaxies. The NIR presents some advantages over the optical regime (Gasparrri et al. 2021); asymptotic giant branch (AGB) and red giant branch (RGB) spectral components can be isolated (the contribution of these populations outside of the K band is negligible) and dust reddening is much reduced in highly obscured galaxies. Absorption line or band indexes can be used to determine stellar populations. These have been studied by e.g. Gasparrri et al. (2021) (following Cesetti et al. 2013 and Morelli et al. 2020). ETGs have specifically been studied by Cesetti et al. (2009) and Riffel et al. (2019).

Studies of composite stellar systems (i.e. galaxies hosting an AGN) often need to subtract the contribution of the underlying galaxy (Cesetti et al. 2009). We use our data set to present an “average” spectrum of objects that do not show any emission lines (79/163 objects). We process the spectra as follows. Each spectrum was smoothed over a 100 pixel boxcar kernel, masking out the

major emission-line regions (He I, Pa γ , Pa β , [Fe II], H₂ and Br γ), plus the CO bandheads above 2293 nm. This smoothed spectrum was divided through the original to create a continuum-normalised spectrum. We then corrected the dispersion solution to account for minor imperfections in the cataloged redshift, by measuring the wavelength of prominent absorption features in the K and H bands; we mainly used the Na I feature at 2207.6 nm. We then averaged the spectra; the result is shown in Figure 3. This plot has been broken up into the $Z+J$, H and K bands. It shows many atomic absorption lines, including Fe I, Al I, C I, Ca I, Na I, Mg I and Si I. Identifications have been obtained from Meyer et al. (1998), Wallace et al. (2000), Rayner et al. (2009), Martins et al. (2013) and Gasparrri et al. (2021). The blue bands highlight those features used as spectral indices, from the work of Gasparrri et al. (2021). We note that the Paschen indices (Pa β and Pa γ) are visible in this stacked spectrum, while the Brackett series is not present. The stacked spectrum also does not show any emission-line activity; in other words there is no low-level, residual emission in these objects. It is well-known that the presence of an AGN dilutes the CO bandheads around 2300 nm, due to the rising hot dust continuum emission (Riffel et al. 2009, 2017). This corresponds to a spectral reddening (flattening), as measured by the $J-K$ colour. We computed this colour from the average flux in a 10 nm window around the effective wavelength of the 2MASS J (1295 nm) and K (2159 nm) filters; this was converted to a magnitude using the NASA/IPAC magnitude/flux density converter² values of the zero-magnitude flux for each filter. We also calculated the CO12 line index using the methodology outlined in Cesetti et al. (2009).

Figure 4 plots the CO12 index equivalent width (in nm) against the $J-K$ magnitude. The points are symbol and colour coded by the IR activity type (as derived in Section 3.4 below). Most galaxies with either no activity or star formation are clumped together, but there is a visible trend with those diagnosed with AGN or LINER activities to have higher $J-K$ values and/or a lower index. The 4 objects with $J-K$ above 1.75 mag are Type 1 Seyferts (IC 450, NGC 5548, UGC 10683) or the Seyfert 2 NGC 2110 with powerful emission lines. The outlying point with a CO12 index = 0.25 and $J-K = 1.2$ is a spectrum with poor S/N. The “Emission” objects are those with any of He I, [Fe II] or H₂, without hydrogen lines to enable nuclear activity classification.

3.2 Emission Features

The spectra were inspected for emission lines and these were measured where found. The lines measured were hydrogen (Pa β and

² <https://irsa.ipac.caltech.edu/data/SPITZER/docs/dataanalysis/tools/pet/magtojy/>

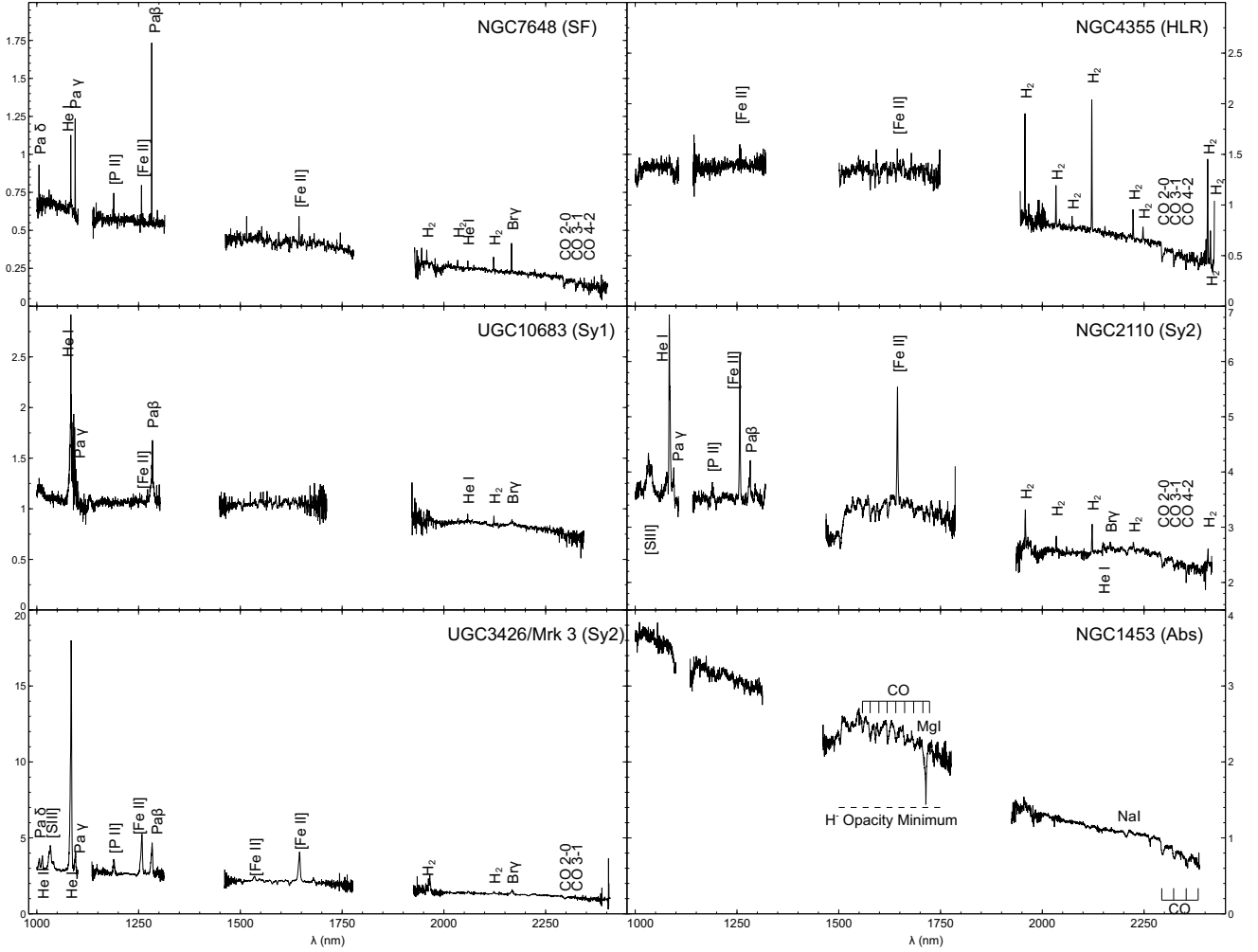


Figure 1. Example spectra, labelled with the galaxy name and activity type (SF - star forming, HLR - high line ratios, Sy1 - Seyfert 1, Sy2 - Seyfert 2, ABS - absorption lines only)

1282 nm and Br γ at 2166 nm), forbidden iron [Fe II] at 1257 nm, H₂ at 2121 nm and He I at 1083 nm. Line identification was usually unproblematic, even with considerable noise.

We used the QFitsView³ (Ott 2012) “de-blending” functionality to fit all emission lines; this allows for both Gaussian and Lorentzian function fits with single or multiple components. This requires some manual input from the user to set the initial estimates of continuum, height, centre and width and uses the GSL⁴ *gsl_multifit* routines, returning fit values and errors of each component (continuum slope, central wavelength, FWHM and flux). Table 3 gives the flux measurement and errors for a sample of objects; the complete list is available online, as described below. All fluxes are given in units of 10^{-16} erg cm⁻² s⁻¹.

The emission lines were usually fitted with a single Gaussian function. In some cases, the permitted hydrogen and He I lines were broad, indicating Seyfert 1 type activity (8/163 objects). In these cases, the lines were fitted with 2 or more Gaussian functions. In

Section 3.3, we analyse these broad lines as the combination of multiple components.

In the spectra of elliptical galaxies presented by M12, approximately 20% of the complete B11 catalog showed Br γ emission, indicating star formation or nuclear activity. In this sample, extended to S0 objects, 50% (82/163) show emission lines, 19% (31/163) show hydrogen lines, with a further 15 having He I flux (without hydrogen emission), indicative of nuclear activity. 38 objects also showed just [Fe II] and/or H₂ emission, indicating HLR activity. In general, hydrogen recombination emission lines are indicative of star formation and/or nuclear activity. In the SF case, the line emission comes from HII regions excited by ionizing photons from massive, young, hot stars, as well as from the stellar atmospheres; another source is from supernova remnants, where the line emission is mainly from the shocked gas. For the infrared lines Pa β and Br γ , single-stellar population models indicate, for an instantaneous starburst, that these have disappeared by 20 Myr; however, for continuous SF, these can persist for > 1 Gyr (e.g. STARBURST99, Leitherer et al. 1999).

³ <http://www.mpe.mpg.de/~ott/dpuser/qfitsview.html>

⁴ <https://www.gnu.org/software/gsl/doc/html/index.html>

17 galaxies had activity classifications from Véron-Cetty &

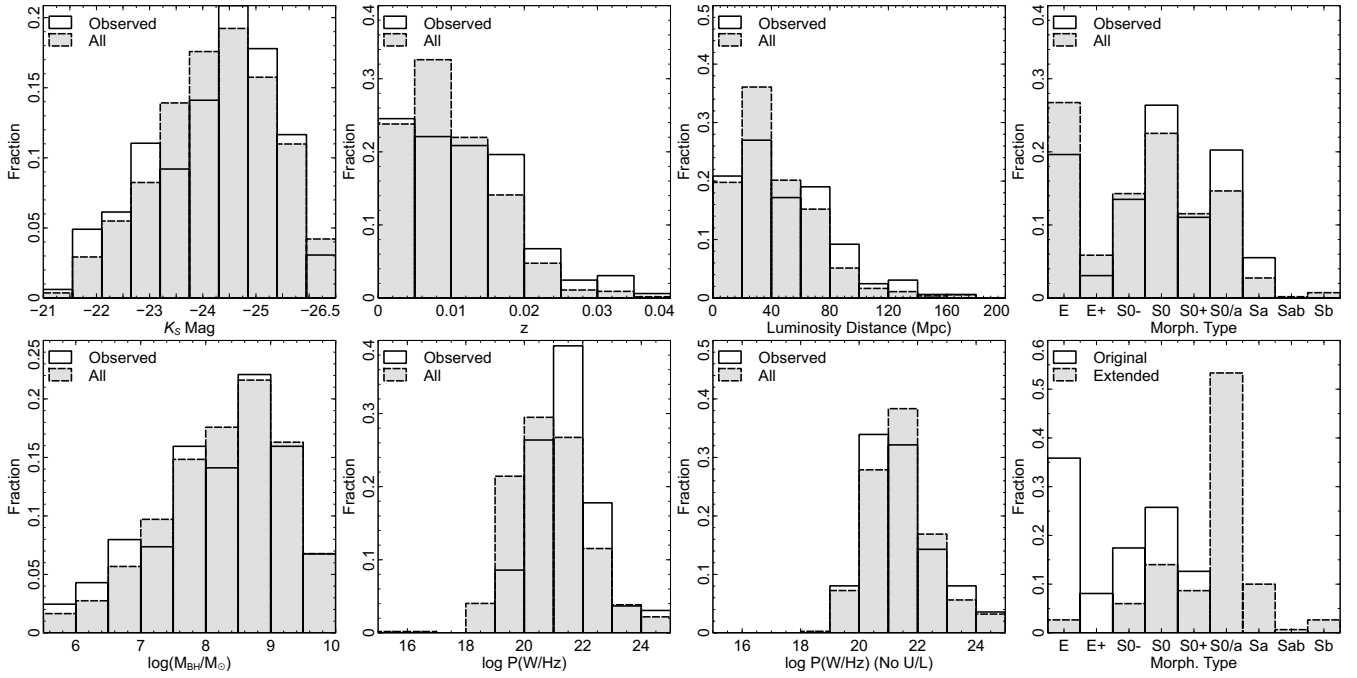


Figure 2. Histograms of absolute K -band magnitude, redshift (z), morphological type and computed black hole mass, for the observed objects vs. the complete catalog.

Véron (2006) and from the SIMBAD Astronomical Database⁵, but showed no measurable emission-line fluxes in the NIR. This can be attributed to poor signal to noise on the measured spectrum; on the other hand, the available optical spectra can be somewhat uncertain.

3.3 Multi-component Emission Lines

For those objects that show multiple components in their emission lines (either from the AGN BLR emission or from multiple NLR components with different velocities - 6/163 objects), we analyse the He I and Pa β lines by fitting a double Gaussian curve. The results are given in Table 4 below. Each object has different characteristics, with the Pa β line in general being the most complex. In all cases the He I line could be fitted with single broad and narrow Gaussian curves.

For NGC 5548 (following Schönell et al. 2017), we fit the Pa β with two broad and one narrow Gaussian curves (with the same for NGC 5273 and IC 450). The Pa β velocity structures are not clear, with the fitted broad components not on the restframe wavelength. The narrow components are at restframe and a relative velocity of ~ -2700 km s $^{-1}$ (IC 450) and ~ -2570 and $+1400$ km s $^{-1}$ (NGC 5548); these can be interpreted as outflows. For IC 450, we were not able to fit the He I line, due to the imperfect subtraction of the telluric OH line at 1097.53 nm. NGC 3516 has 3 prominent Pa β narrow lines superimposed on the broad line. While UGC 3426 (Mrk 3) has broader lines than standard narrow-line width (~ 525 km s $^{-1}$), this is not a classic broad-line region, as the permitted and forbidden lines are the same width; the line profiles are caused by powerful outflows of ionised gas. In Table 4, where there are multiple components, the fluxes are the sum of all components.

Figure 5 gives examples of Gaussian component fits to the

broad Pa β emission line for NGC 5548 and IC 450, with the object spectrum, the individual components and the residuals.

3.4 Nuclear Activity Diagnostics

Nuclear activity for NIR emission line objects can be categorized by a diagnostic diagram (Larkin et al. 1998; Rodríguez-Ardila et al. 2005), where the log of the flux ratio H $_2$ /Br γ is plotted against that of [Fe II](1257 nm)/Pa β . This is analogous to the BPT diagrams (Baldwin et al. 1981) commonly used in the optical regime (e.g. Kewley et al. 2006). Following the updated limits from Riffel et al. (2013), the diagram is divided into three regimes for star formation/starburst (SF; dominated by H II regions), AGN (subjected to the radiation field from the accretion disk), and high line ratio (HLR) excitation, where shocks from supernovae (SNe) and evolved stellar outflows dominate. We follow Riffel et al. (2021a) for the HLR nomenclature, as it encompasses transition objects, LINERs and supernovae remnants. It is noted that nuclear activity can be apparent even though the galaxy may not be classified with a catalogued activity type from Véron-Cetty & Véron (2006).

These ratios are plotted in Figure 6 for those objects with measurable flux for all 4 lines. 26 of the 163 objects in our sample are detected with all these emission lines. A further 5 galaxies showed no Br γ emission, but it could be calculated from the Pa β flux using the Hummer & Storey (1987) canonical ratio of Br γ /Pa β = 5.85 (for $T_e = 10^4$ K and $n_e = 10^3$ cm $^{-3}$); this assumes no significant extinction. For those galaxies with multiple component broad-line emission, we used the narrow Pa β and Br γ components. Three of these galaxies (NGC 3516, NGC 5273 and NGC 5548) showed no broad Br γ emission with weak or no narrow emission; given the Pa β fluxes, these should have been visible. Over the standard range of ISM temperatures (500-30000 K) and densities ($n_e = 10^2 - 10^7$ cm $^{-3}$), the Pa β /Br γ ratio varies ~ 5 -6.5. Higher-level hydrogen line

⁵ <http://simbad.cds.unistra.fr/simbad/>

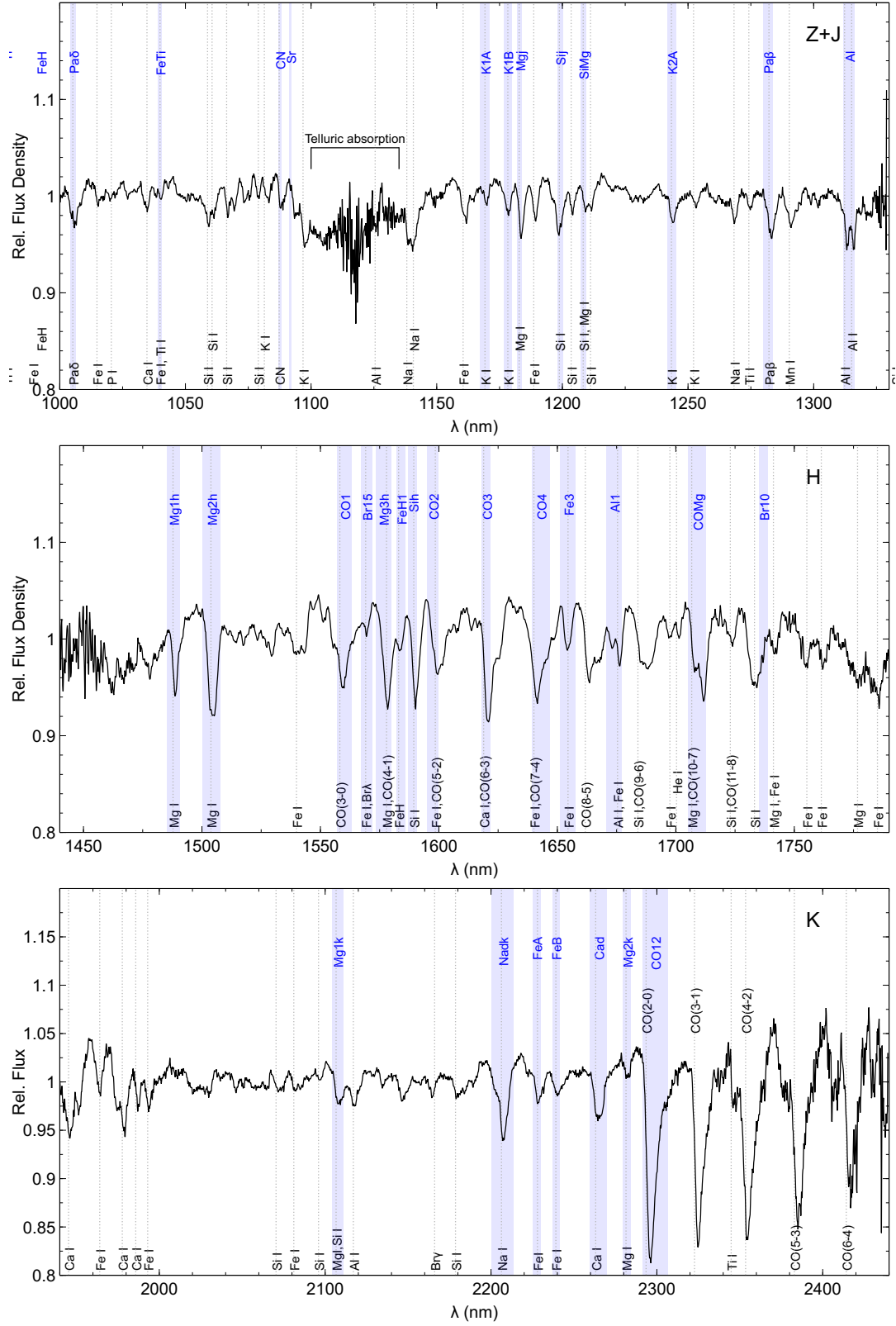


Figure 3. Stacked normalised spectrum (from objects with no emission lines) showing the main absorption features. The blue bands highlight the spectral indices, named with blue text, as discussed in the text.

Table 3. Sample of emission-line fluxes for the main atomic and ionised species, in units of 10^{-16} erg cm^{-2} s^{-1} . $E(B - V)$ is calculated from the Pa β /Br γ flux ratio, as discussed in section 3.6. (The full table is available online)

Object	He I (1083 nm)	[Fe II] (1257 nm)	Pa β (1282 nm)	H ₂ (2121 nm)	Br γ (2166 nm)	$E(B - V)$ (mag)
2MASX J20173144+7207257	34.5±3.3	23.3±2.2	41.8±1.9	10.7±1.2	12.7±1.5	1.16
ESO483-12	20.4±6.9	24.0±9.9	36.3±6.0	17.1±1.4	13.1±1.3	1.93
ESO507-25	56.7±32.6	25.4±10.0	...	43.4±3.1	...	
IC0051	15.2±1.8	49.6±0.9	18.6±1.1	2.9±0.3	3.7±0.7	0.35
IC0450	...	514.0±5.3	967.6±134.4	76.7±10.0	71.1±10.8	-2.34
IC0537	...	54.2±16.3	...	52.8±5.2	...	
IC0630	4470.0±67.6	339.0±16.3	2010.0±37.1	37.4±2.9	536.0±9.6	1.13
MCG-01-29-015	21.6±1.0	...	
MCG-02-33-017	23.6±4.2	
MCG+04-50-004	381.0±4.6	21.8±4.4	50.4±32.0	24.8±1.6	...	
MRK612	172.9±13.1	82.4±6.2	58.6±6.9	37.5±2.8	15.4±2.7	1.09
NGC0051	...	28.7±6.7	...	35.6±2.1	...	
NGC0383	...	6.4±2.1	
NGC1052	389.0±24.9	342.0±16.0	...	33.2±3.3	...	
NGC1222	753.0±6.3	81.7±3.5	493.0±7.0	18.7±2.7	167.0±5.2	1.76
NGC2110	814.0±38.8	588.0±12.3	59.0±7.1	107.0±35.6	23.3±3.9	1.89
NGC4438	114.0±28.5	215.0±18.3	37.5±5.2	174.0±7.4	...	
NGC5273	1125.0±51.2	31.0±3.4	7.5±4.9	32.2±1.8	...	
NGC5548	4810.0±76.6	22.8±5.7	58.1±7.5	11.4±1.9	10.5±2.5	0.13
NGC7465	707.0±81.0	213.0±10.9	178.0±12.0	84.7±7.2	23.0±5.3	-0.80
UGC3426	4700.0±200.0	1210.0±36.0	809.0±36.1	42.8±4.5	174.0±8.7	0.45
UGC5745	41.9±9.1	62.9±5.8	51.2±6.0	16.0±3.1	15.7±2.3	1.49

Table 4. He I and Pa β parameters for objects showing multiple components in emission. (This table is available online).

Object	He I (b)			He I (n)			Pa β (b)			Pa β (n)			Notes
	Flux★	λ †	W‡	Flux	λ	W	Flux	λ	W	Flux	λ	W	
NGC 3516	38.9±1.6	1083.5	14.3	6.8±0.5	1083.4	2.7	11.8±0.8	1280.5	13.1	1.3±0.2	A
NGC 5273	11.4±0.5	1084.3	17.2	1.0±0.1	1083.8	0.9	5.7±0.7	0.4±0.1	1278.1	2.2	B
NGC 5548	46.7±0.8	1084.3	27.8	7.2±0.2	1083.8	2.1	23.9±0.6	0.6±0.1	1282.8	1.9	C
NGC 7465	7.8±0.6	1083.4	4.6	2.8±0.2	1083.3	0.9	4.3±0.4	1281.6	6.0	1.8±1.1	1281.9	0.9	
UGC 10683	6.2±0.8	1083.7	11.7	1.8±0.2	1083.7	3.4	2.2±0.4	1283.2	9.8	0.4±0.1	1283.3	2.6	
IC 0450	18.0±3.0	9.7±1.3	1281.6	6.6	D

Notes:

- ★ Flux in units of 10^{-14} erg cm^{-2} s^{-1} .
- † Restframe wavelength of Gaussian fit in nm.
- ‡ Full-width half maximum in nm.
- A Pa β narrow line flux total of 3 components at 1279.03, 1282.10, 1287.18 nm.
- B Pa β broad line 2 components at 1282.34, 1300.01 nm.
- C Pa β broad line 2 components at 1270.37, 1289.09 nm.
- D He I line affected by telluric skyline. Pa β broad line 2 components at 1271.69, 1290.52 nm.

emission can be suppressed in the extreme conditions of the AGN (McAlary et al. 1986; Hubbard & Puetter 1985), e.g. at $T_e = 10^3$ K and $n_e = 10^{14}$ cm^{-3} , the ratio is ~ 33.5 (e.g. Cutri et al. 1984, for Mrk 231). For UGC 3426 (Mrk 3), we use the full flux value, as the multiple components and broad lines are caused by powerful outflows (as seen in the similar line widths for narrow lines e.g. [Fe II] and H₂).

Of these 31 galaxies, 4 are classified in the IR regimes as SF, 24 as AGN and 3 as HLR. The corresponding optical classification is plotted for each object as symbols and colours. The general correlation between the $\log(H_2/Br\gamma)$ and $\log([Fe II]/Pa\beta)$ is apparent; the orthogonal linear fit is:

$$\log([Fe II]/Pa\beta) = 0.634 \log(H_2/Br\gamma) - 0.186 \quad (1)$$

This is plotted in Figure 6 with 95% confidence bands. This is

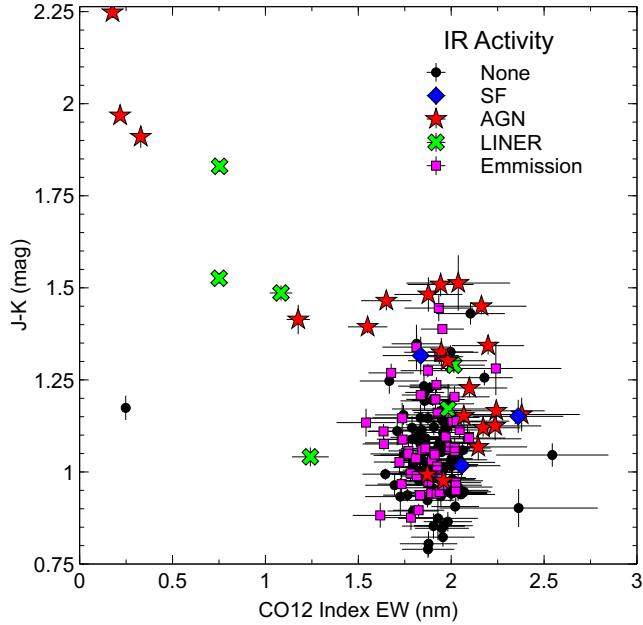


Figure 4. CO12 absorption line index vs. $J - K$ colour, symbol and color coded by the IR nuclear activity. This shows a trend with nuclear activity producing a weaker CO12 index and a redder (flatter) continuum

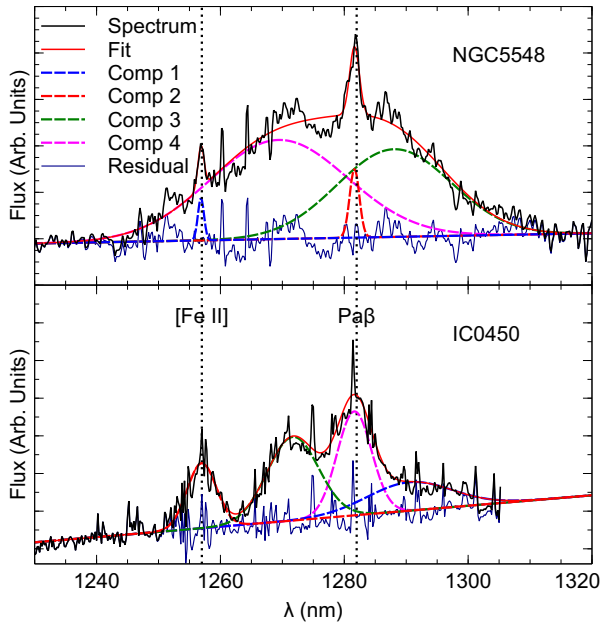


Figure 5. Examples of multiple Gaussian curve fits to Seyfert 1 line profiles for NGC 5548 and IC 450.

comparable with the fit found by Riffel et al. (2013) (their Figure 8, plotted on Figure 6 as a dashed red line). 4 objects have no optical classification, 13 are SB/HII/SBG, 5 are Sy1/Sy1.5, 6 are Sy1.9/Sy2 and 3 are LINERS.

The plot also includes those objects with no visible hydrogen lines. These are plotted using the upper limits of $\text{Pa}\beta$ and $\text{Br}\gamma$.

These are mostly in the HLR region and are colour-coded with optical activity type. The great majority of these are LINERS.

Originally, 11 of these galaxies had no classification from Véron-Cetty & Véron (2006) or NED (the NASA/IPAC Extragalactic Database)⁶. 7 of these were found to have optical spectra available from NED; the diagnostic lines ($\text{H}\alpha$, $\text{H}\beta$, $[\text{N}\text{II}]$, $[\text{S}\text{II}]$ and $[\text{O}\text{III}]$) were measured and the object classified according to the Kewley et al. (2006) diagrams, with 5 SF/HII and 2 Sy galaxies. 6 galaxies are classified by SIMBAD as "EmG", i.e. emission-line galaxies. These were also re-measured and found to be 4 SF, 1 Sy and 1 LINER.

In general, the optical and IR diagnostics are reasonable well matched, however, it is not perfect. 10 (of 14) optical SF/HII galaxies are in the IR AGN or HLR regimes; this is most likely due to the dust obscuration of the nucleus which is penetrated in the IR revealing the AGN; the optical SF diagnostic would then be from unobscured SF regions away from the nucleus. One galaxy (NGC 7465) was optically classified as a LINER, but shows broad HeI , $\text{Pa}\beta$ and $\text{Br}\gamma$ emission lines. Measurement of its NED spectra re-classifies it as a Seyfert 2, which is then revealed as Seyfert 1 in the IR. The spectra of all the optical SF galaxies were checked as before, and found to be truly SF, except for NGC 3593, which was reclassified as a Seyfert 2. The changed classifications are flagged in the complete catalog, as described in Section 4.

Similarly, two galaxies (NGC 5273 and NGC 7465) change classifications from Seyfert 1.9 and Seyfert 2 (respectively) to full-blown Seyfert 1 galaxies. Similar examples are found in Reunanen et al. (2002).

We also plot the overall excitation diagnostic for all 31 galaxies, by stacking the spectra as described in Section 3.1. This plotted as a black cross (Stacked), located in the AGN regime.

Objects with no H lines are marked with upper limit arrows, using the same colour code for optical activity type. The ratios are calculated using the upper limits of $\text{Pa}\beta$ and $\text{Br}\gamma$, derived as described before.

3.5 Molecular Hydrogen

Molecular hydrogen (H_2) is very important in the star formation context of AGN activity, since it is the basic building block for stars. In the K -band, there are a series of rotational-vibrational emission lines, which can be used to examine the excitation mechanism for H_2 ; this can be either UV photons (fluorescence) from star formation and/or AGN continuum emission (Black & van Dishoeck 1987), shocks from SNe, AGN outflows, star formation winds (Hollenbach & McKee 1989) or X-rays from the AGN irradiating and heating dense gas (Maloney et al. 1996). The distribution and excitation mechanisms for individual galaxies has been studied extensively (e.g. Mouri 1994; Quillen et al. 1999; Davies et al. 2003; Rodriguez-Ardila et al. 2005; Wilman et al. 2005; Riffel et al. 2008, 2021b), especially in the context of active galaxies. Here we examine the bulk properties of the molecular gas from our sample.

Following the method outlined in Wilman et al. (2005), for gas with density $n_T > 10^5 \text{ cm}^{-3}$, the thermal (collisional) temperatures can be estimated. The occupation numbers of the excited ro-vibrational levels of the H_2 molecule will be in thermal equilibrium at a temperature T_{exc} equal to the kinetic temperature of the

⁶ <http://ned.ipac.caltech.edu/>

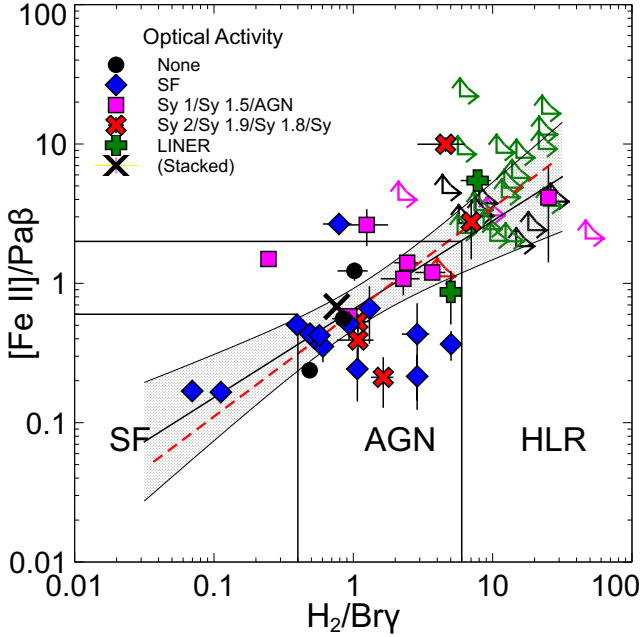


Figure 6. Infrared excitation diagram with the regimes from Riffel et al. (2013) delineated, as discussed in the text. The emission line flux ratios $[\text{Fe II}]/\text{Pa}\beta$ vs $\text{H}_2/\text{Br}\gamma$ are plotted for those objects with measurable flux for all 4 lines. The optical activity type is coded by a symbol and colour as given in the legend, and matches the IR diagnostic well. The diagnostic point from stacking all emission-line spectra is the black cross symbol (Stacked). 10 galaxies optically classified as SF are revealed as “hidden” AGN or LINERs in the IR diagnostic. The correlation is similar to that found by Riffel et al. (2013); their fit (dashed red line) compares to that found here (orthogonal linear fit as a black line with 95% confidence interval). Objects with no H lines are marked with upper limit arrows, using the same colour code for optical activity type; these are mostly LINERs.

gas. This leads to the relationship:

$$\ln N_{upper} = \ln \left(\frac{F_i \lambda_i}{A_i g_i} \right) = \text{constant} - \frac{T_i}{T_{exc}} \quad (2)$$

where $\ln(N_{upper})$ is the occupation number of the upper level of the H_2 transition, F_i is the flux of the i th H_2 line, λ_i is its wavelength, A_i is the spontaneous emission coefficient, g_i is the statistical weight of the upper level of the transition and T_i is the energy of the level expressed as a temperature. This relation is valid for thermal excitation, under the assumption of an *ortho:para* abundance ratio of 3:1. The values of λ_i , A_i , g_i and T_i were obtained from the Gemini observatory online data resource “Important H2 Lines”⁷, with the values updated from Roueff et al. (2019)⁸.

69 galaxies (42% of 163) show H_2 2121 nm emission; to find an “average” temperature we stacked all the spectra, each normalised as described in section 3.1. Each spectrum was weighted in the stacking process by the continuum flux, averaged over the wavelength range 2130–2145 nm. This is then divided though by the stacked absorption spectrum (see Section 3.1) to remove absorption-line features. The resulting *K*-band emission line sequence is shown in Figure 7.

⁷ <https://www.gemini.edu/observing/resources/near-ir-resources/spectroscopy/important-h2-lines>

⁸ <http://cdsarc.u-strasbg.fr/viz-bin/cat/J/A+A/630/A58>

The lines are marked with their transition notations; for a transition $\nu_u, J_u \rightarrow \nu_l, J_l$ (where $\nu_u, J_u; \nu_l, J_l$ are the upper (u) and lower (l) level of the vibrational and rotational quantum numbers), is notated $\nu_u - \nu_l X(J_l)$, where “X” is one of S, Q or O, depending whether J is changed by $-2, 0$ or $+2$, respectively. For example, for the H_2 2121.8 nm line, the transition is 1-0 S(1), with $\nu_1, J_3 \rightarrow \nu_0, J_1$.

In spectrum plot (Figure 7), the hydrogen Br γ (2166 nm), Br δ (1945 nm) and He I (2058 nm) emission lines are also visible.

Measuring the relative fluxes from the $\nu=1-0$ and $2-1$ sequences, we fit a straight line to the calculated $\ln(N_{upper})$ plot; the negative inverse of the slope gives the temperature. Fitting the values (as shown in Figure 8), gives a temperature of 1957 ± 182 K. If we just fit the low-excitation lines ($\nu=1-0$), the temperature is lower (904 ± 85 K). This can be due to several factors; (1) the high excitation lines ($\nu=2-1$) are weak, with corresponding uncertainties, (2) the warm H_2 gas is not homogeneous with a smaller gas mass being hotter and (3) Davies et al. (2003, 2005) showed that the low-excitation levels may be thermalized, but the higher levels can be overpopulated owing to fluorescent excitation by far-ultraviolet photons.

We can examine whether various parameters affect the H_2 temperature, by splitting the spectra into 2 bins. The results are given in Table 5. As the measurement of the $2-1$ transitions is uncertain due to weak emission lines, we will concentrate on the temperature computed from the $1-0$ transitions only. For radio power, the bin break is at $\log P$ (W Hz^{-1}) = 21.5. Contrary to expectations, the higher radio power group has a significantly lower temperature than the lower power group; for both all and $1-0$ transitions measurements, the 2-sided t-test for the slopes gives a significance $p = 0.0006$ and $p < 0.0001$ respectively. There is no difference in temperature when we split by H_2 luminosity with the break at $\log L$ (erg s^{-1}) = 38.5 ($p = 0.29$ and $p = 1$). Table 5 also gives the result for the galaxy with the highest H_2 flux, NGC 4355, which has a somewhat higher temperature than the averaged value.

These temperatures are lower than those found for Seyfert galaxies observed with integral field spectroscopy (IFS), in the range 2100–2700 K (e.g. Riffel et al. 2015; Storchi-Bergmann et al. 2009; Riffel et al. 2014; Riffel & Storchi-Bergmann 2011; Riffel et al. 2010; Durré & Mould 2018). This is probably due to the spectroscopic slit encompassing cooler molecular regions than the higher resolution IFS observations, plus a large fraction of the galaxies not being AGNs.

The dominating excitation mechanism of H_2 can be estimated and the contributing fractions of different mechanisms can be constrained (Busch et al. 2017). We use the methods of Mouri (1994), calculating the rotational and vibrational temperatures from the $[1-0 \text{ S}(0)]/[1-0 \text{ S}(2)]$ and $[2-1 \text{ S}(1)]/[1-0 \text{ S}(1)]$ flux ratios, respectively. Figure 8 right panel (after Mouri 1994 and Krabbe et al. 2000), plots excitation models, following Riffel et al. (2021b) (models from Kwan 1977; Black & van Dishoeck 1987; Sternberg & Dalgarno 1989; Draine & Woods 1990; Mouri 1994; Smith 1995; Davies et al. 2003; Dors Jr et al. 2012, see Riffel et al. 2021b Figure 8 for details). The ratios from the flux weighted measurements of all objects with H_2 emission is plotted, along with that for NGC 4355, which has the highest H_2 flux of the sample. These are both in the thermal regime, with a mixture of UV photons and shocks as the driving mechanisms.

3.6 Extinction

We can use the emission-line ratio $\text{Pa}\beta/\text{Br}\gamma$ as an extinction diagnostic. In general, the extinction km s^{-1} is calculated from the ratio

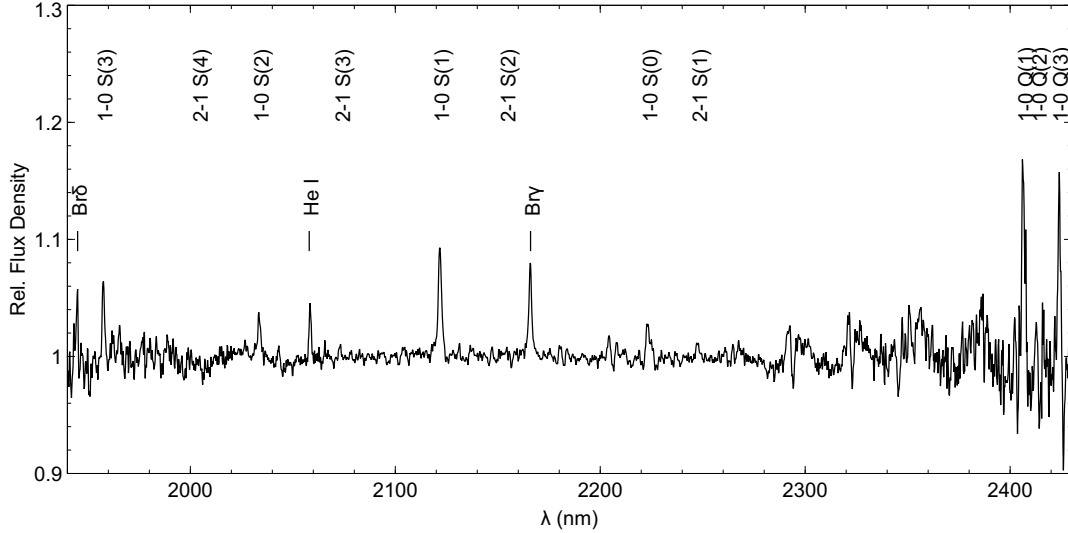


Figure 7. Stacked normalised spectra that have non-zero H_2 flux, weighted by the continuum 2130–2145 nm. The emission lines are marked with the transition notation, including the prominent $Br\gamma$, $Br\delta$ and $He\ I$ lines. The 1-0 S and Q lines are prominent, with the higher excitation 2-1 S lines much weaker.

Table 5. H_2 temperatures, measured from K -band emission line sequence. As well as for all galaxies with H_2 emission (weighted by the continuum flux), the objects are binned by low/high radio power and low/high H_2 luminosity. NGC 4355 is included as the brightest H_2 flux object. The table shows the object count, the temperatures for both the 1-0 and 2-1 transitions and the 1-0 transitions only, and the T_{Vib} and T_{Rot} temperatures (all in K).

Method	#	Temp. (All)	Temp. (1-0)	T_{Vib}	T_{Rot}
All	69	1957 ± 182	904 ± 85	2882 ± 408	996 ± 69
Radio power $\log P < 21.5$	33	1950 ± 144	882 ± 65	2710 ± 568	1028 ± 206
Radio power $\log P \geq 21.5$	36	1690 ± 124	642 ± 19	2097 ± 809	710 ± 91
H_2 luminosity $\log L < 38.5$	34	1985 ± 203	737 ± 66	3324 ± 1075	775 ± 178
H_2 luminosity $\log L \geq 38.5$	35	1855 ± 270	773 ± 50	2012 ± 379	970 ± 101
NGC4355	1	2080 ± 91	1369 ± 68	2357 ± 223	1384 ± 78

of the flux of two hydrogen species using the formula:

$$E_{B-V} = \alpha \log \left(\frac{\beta}{f_1/f_2} \right) \quad (3)$$

where f_1, f_2 are the fluxes of species 1 and 2 (in this case $Pa\beta$ and $Br\gamma$), α is a constant depending on the extinction law and the wavelengths of the two species and β is the intrinsic ratio of the fluxes given the physical conditions of the emitting region. We use the canonical ratio (as above) of $\beta = 5.86$ and the Cardelli et al. (1989) extinction law, giving $\alpha = 6.07$. The results are given in Table 3, for 25 objects where both $Pa\beta$ and $Br\gamma$ were measurable. The values were corrected for galactic extinction, using data from the IRSA Galactic Dust Reddening and Extinction service⁹ using the Schlafly & Finkbeiner (2011) values; these were in the range 0.014–0.36 mag $E(B-V)$. The extinction varies from 0.13–2.58 mag $E(B-V)$; however 3 objects display anomalous “negative” extinctions. These are Seyfert 1 objects (IC 450, NGC 7465 and UGC 10683) where $Br\gamma$ is suppressed due to the extreme gas densities found in the BLR; this is further discussed in Sections 3.3 and 3.4.

3.7 NIR and Radio Emission Correlations

We explore the correlations between the radio and various emission-line luminosities. Figure 9 shows the plots of the radio luminosity on

the X-axis vs. each emission line luminosity (Y-axis) as labelled on each panel (black points). We also include the plot for the emission-line upper limits (blue upper-limit arrow markers); these limits are calculated from the 3σ standard deviation over a 5 nm range around the line wavelength, with the continuum fitted locally with a third-order polynomial. In a few cases, both emission line luminosity and radio power have upper limits; these are marked with red symbols. Note there are no cases where there is a measured emission-line luminosity with a radio power upper limit. We plot the orthogonal linear regression fit. We note that while the $Pa\beta$ and $He\ I$ fits have slopes ≥ 1 , the $[Fe\ II]$ and H_2 fits are sub-linear. For molecular hydrogen, specifically, this means that at higher radio power, the AGN is emitting relatively less thermal energy from UV and X-rays and more radio power. This could provide an explanation of the lower H_2 temperatures found at higher radio power, as noted in Section 3.5.

While there is a trend with radio power of the emission-line luminosities, the upper limits are also, in general, showing the same trend; we therefore cannot couple them directly. While radio emission is always present (by sample selection), NIR line emission is not. This indicates that the duty cycles of SF and AGN activity are not synchronised. This has been explored in simulations, showing AGN activity triggering SF (Zubovas et al. 2013; Zubovas & King 2019), as well as in the reverse direction (e.g. Schartmann et al. 2017), where Toomre-instability induced nuclear SF can cause AGN activity though stellar outflows. Davies et al. (2007, 2009) ob-

⁹ <https://irsa.ipac.caltech.edu/applications/DUST/>

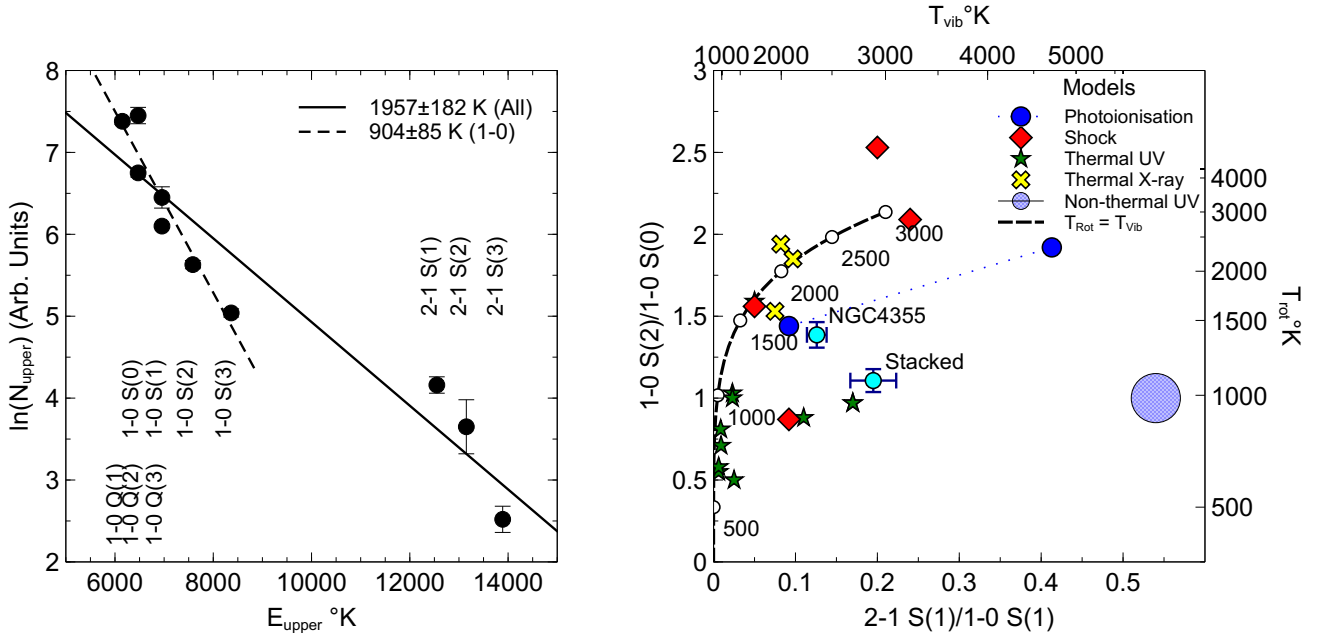


Figure 8. Left panel: H_2 temperature plot. The value of the inverse slope of the relationship between $\ln(N_{\text{upper}})$ and E_{upper} is the excitation temperature (T_{exc}) of H_2 . We distinguish between all 2-1 and 1-0 transitions, vs. only those of the 1-0 transition. The transition notations are labelled, and the slopes with their corresponding temperatures given in the legend. Right panel: Excitation mechanism plot after (Mouri 1994) and Riffel et al. (2021b), showing that the excitation is a mixture of thermal UV and shock mechanisms. Various excitation models are plotted, as described in the text.

serve moderately recent (10–300 Myr) starbursts their sample of AGNs, deducing episodic periods of SF and positing a 50–100 Myr delay between SF and AGN activity onsets. They concluded that OB stars and supernovae (SNe) produce winds that have too high velocities to feed the AGN, but that evolved AGB stellar winds with slow velocities can be accreted efficiently onto the super-massive black hole (SMBH).

Ogle et al. (2010) found far infrared (FIR) warm molecular hydrogen emission from 17/55 (31%) of a sample of radio galaxies, which compares to 42% (69/163) of our sample. They suggest that their class of radio-selected molecular hydrogen emission galaxies (radio MOHEGS) is powered by radio-jet feedback in the form of kinetic energy dissipation by shocks or cosmic rays. However, their galaxies are nearly all members of clusters or close pairs (contrary to our sample) suggesting the H_2 is delivered in galaxy collisions or cooling flow.

We also correlate NIR emission line luminosities with each other; Figure 10 shows the plots of $\text{Pa}\beta$ vs. He I , $[\text{Fe II}]$ and H_2 , as well as $[\text{Fe II}]$ vs. H_2 . These all show strong correlation with each other, and display the trend of line strength vs. radio power, as color-coded for each marker. We note the particularly strong association between $\text{Pa}\beta$ and He I , especially at higher powers; this indicates that the excitation mechanisms for both species are very similar. The higher emission powers are almost certainly due to AGN activity; as these galaxies are early types, their SF rate is expected to be low. As an indication, a SF rate of $1 M_{\odot} \text{ yr}^{-1}$ will produce a $\text{Pa}\beta$ luminosity of the order of $10^{40} \text{ erg s}^{-1}$ (Kennicutt 1998). Similarly, using the relationship in Brown et al. (2017) between radio power and $\text{H}\alpha$ luminosity, with $\log(P) = 21$, the SFR (without any AGN contribution) is $0.63 M_{\odot} \text{ yr}^{-1}$.

3.8 Aperture Effects and Emission Line Detection Rates

The Triplespec spectrograph slit was set to $1''$, and the data reduction pipeline used a $3''$ extraction aperture. At a distance of 1 Mpc, this scales to a window $\sim 5 \times 15$ pc; our objects range in distance 7.4 – 167 Mpc, i.e. window ranges of 37×111 pc – 850×2505 pc. This could have an effect on detection, as the nuclear emission lines get diluted by increased galactic light with distance. As the integration time is mostly the same for all galaxies, further galaxies, being fainter in general, will decrease the S/N for each observation, again decreasing detectability.

From the emission line measurements, the lowest flux detection for $\text{Pa}\beta$ is about $7.5 \times 10^{-16} \text{ erg cm}^{-2} \text{ s}^{-1}$. It is somewhat lower for H_2 , which is due to the continuum having better S/N in that wavelength region. Plotting $\text{Pa}\beta$ luminosities and upper limits against luminosity distance (Figure 11 - left panel), we can see that there are no detections above 100 Mpc; this is beyond the nominal limit of 75 Mpc of M12. We also plot the expected luminosity lower limit, given the flux detection limit. We also plot the histogram of detected vs. non-detected fractions of $\text{Pa}\beta$ at 25 Mpc intervals (Figure 11 - right panel), showing the fraction of detections for both all objects and those above the flux lower limit. The error bars are computed using Gehrels’s approximation for small numbers (Gehrels 1986); no definitive bias with distance is visible. The $\text{Pa}\beta$ detection rate for all objects is 19.6%, if we exclude those objects below the flux detection threshold, this increases to 26.7%.

If non-nuclear emission were significant, we would expect a bias on Figure 6 towards the left and down, i.e. for increasing SF. However, we see no such bias; our sample is largely confined to early-type galaxies, where we would not expect significant non-nuclear star formation. Similarly, the line index measurements (Figure 4) show no bias with distance.

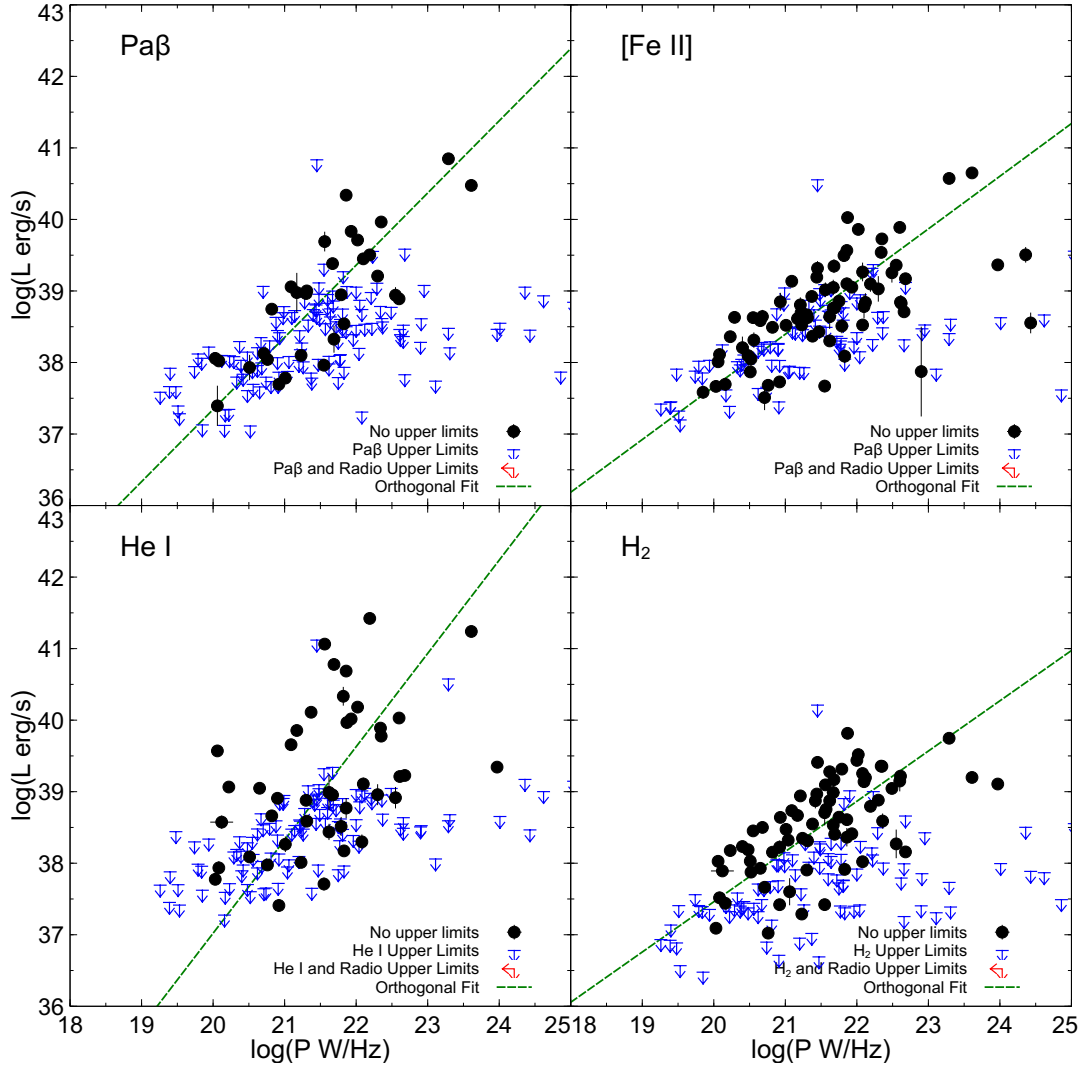


Figure 9. Correlation of radio power (X-axis) with NIR emission-line luminosities (Y-axis). The particular species is given in each panel, with black dots denoting firm measurements, blue symbols represent upper limit on the NIR fluxes and red symbols where both radio and NIR emission has upper limits. The orthogonal linear regression fit is also plotted.

4 THE COMPLETE “RADIO ACTIVE” CATALOG

The complete catalog of radio galaxies (including the observed targets of “opportunity”) has the object name and alternate ID (the primary identifier from SIMBAD or the NASA/IPAC Extragalactic Database (NED)¹⁰ if not the same), the position and redshift, the K -band relative and absolute magnitude, the activity type and the morphology. The data in the original catalog has been extended to include the central velocity dispersion (σ) from the HyperLeda database¹¹ (Makarov et al. 2014) (440 objects) or from the SDSS spectroscopic data (11 objects) (Abdurro’uf et al. 2022; Smee et al. 2013).

The morphological types (T type) have been consolidated to the nearest integer (e.g. an original type of -3.3 is now set to -3). The SMBH mass (M_{\bullet}) is calculated from either σ or from the K -band magnitude (where σ is not available). The formula for the

Table 6. Parameters for Equation 4.

Morphology	T type	α	β
With a disk (ES, S0, Sp types)	T \geq -3	5.72	8.22
Without a disk (E type)	T \leq -4	6.69	8.65

relationship between σ and M_{\bullet} is given by :

$$\log(M_{\bullet}) = \alpha + \beta \log\left(\frac{\sigma}{200}\right) \quad (4)$$

where σ is given in km s^{-1} and the parameters depend on the morphological type, as given by Sahu et al. (2019) (Table 6).

If σ is not available, then M_{\bullet} is calculated from the formula presented by Graham & Scott (2013) (from their Table 4), which is a broken power law:

$$\log(M_{\bullet}) = 9.05 - 0.44 \times (M_K + 25) \quad (M_K < -23.36) \quad (5)$$

$$= 7.39 - 1.09 \times (M_K + 22.5) \quad (M_K \geq -23.36) \quad (6)$$

Radio data for the extended catalog is mostly from the NRAO VLA Sky Survey (NVSS) (Condon et al. 1998) at 1.4 GHz, as

¹⁰ <http://ned.ipac.caltech.edu/>

¹¹ <http://leda.univ-lyon1.fr/>

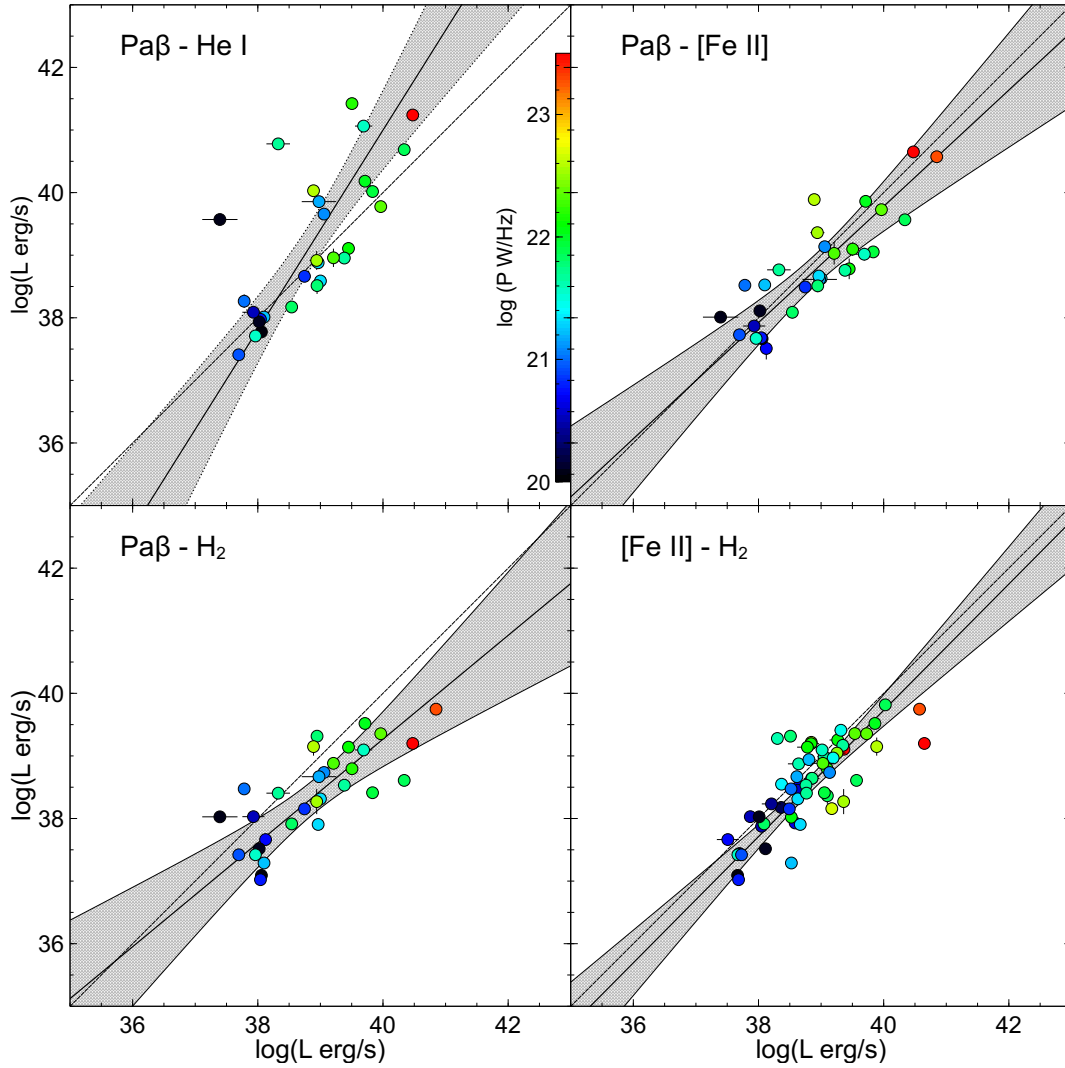


Figure 10. Correlations between NIR species luminosities. The X- and Y-axes species are given in each panel. The markers are colour-coded by radio power, as given in the colour-bar. The orthogonal regression fit is also plotted, with 95% confidence bands.

described in B11, without any supplementary observations (525 objects in total). Where this was not available, data was taken from (in preference order) the VLA FIRST survey (2 objects, Becker et al. 1995) at 1.4 GHz, the Arecibo 2.38 GHz survey of bright galaxies (5 objects, Dressel & Condon 1978), the Sydney University Molonglo Sky Survey (SUMSS) at 843 MHz (Mauch et al. 2003, 12 objects), the Parkes-MIT-NRAO catalog at 4.85 GHz (1 object, Gregory et al. 1994) and (1 object, Whiteoak 1970) at 5 GHz. One object (NGC 6831) had no radio flux information in the NASA/IPAC Extragalactic Database (NED).

Distances were found from either the COSMICFLOWS-3 catalog (Tully et al. 2016) or from the object redshift. The luminosity distance is computed from the distance using the functionality implemented in TOPCAT¹² (Taylor 2005), which depends on the cosmological parameters given above, and is subsequently used to calculate NIR and radio luminosities. The 2MASS (Skrutskie et al. 2006) *K*-band absolute magnitude and distance are taken from the full table of data from B11.

Morphological (T) type is taken from the Third Reference Catalog of Bright Galaxies (de Vaucouleurs et al. 1991). Nuclear activity is taken from “A catalogue of quasars and active nuclei: 12th edition” (Véron-Cetty & Véron 2006) or, alternately, from SIMBAD (object type) or NED data (activity type). These have been consolidated somewhat into the following values: Sy - Seyfert (not sub-categorised), Sy1/Sy1.5/Sy1.8/Sy1.9/Sy2 - Seyfert with sub-category, LIN - LINER, HII - H II, SBG - star-burst, AGN - AGN, QSO, blazar, BL Lac etc. (without further characterisation), Em - galaxies with emission lines but otherwise unclassified.

The catalog also lists other optical and NIR surveys for each object with either spectroscopy or IFU observations. These are listed in the “Surveys” column in Table 7, with counts of matched objects.

5 CONCLUSIONS

We have presented a near infrared spectroscopic atlas of nearby, bright early-type galaxies with radio emission, containing 163 galaxies observed by the Palomar 200” TripleSpec instrument. We explore the science goals enabled by these observations. We have

¹² <http://www.star.bristol.ac.uk/~mbt/topcat/>

Table 7a. Sample of the catalog of “Radio Active” galaxies, extending the B11 catalog - Part 1. (The full table is available online)

Galaxy (1)	Alt. ID (2)	Catalog (3)	RA (4)	Dec (5)	z (6)	m_K (7)	M_K (8)	D (9)	Ref (10)	D_L (11)	σ (12)	Ref (13)
2MASX J16251687-0910524		3	246.3204	-9.1811	0.02861	10.20	-25.20	117.6		120.1		
IC0450	Mrk 6	2	103.0514	74.4270	0.01302	9.56	-24.90	76.8		77.9		
IC5063		2	313.0097	-57.0688	0.01127	8.75	-24.59	46.3		46.6	152.3	
NGC0080		1	5.2951	22.3571	0.01895	8.92	-25.71	83.2	C	84.5	248.4	
NGC0447		2	18.9069	33.0678	0.01885	9.48	-25.00	77.5		78.6	157.8	
NGC1052		1	40.2700	-8.2558	0.00493	7.45	-23.94	19.0		19.0	208.0	
NGC1316		1	50.6741	-37.2082	0.00591	5.59	-26.03	21.0	C	21.0	223.1	
NGC2217		1	95.4156	-27.2338	0.00543	7.09	-24.94	25.5	C	25.5	216.1	
NGC3182		2	154.8876	58.2057	0.00706	9.47	-22.84	29.0		29.1	112.7	S
NGC3593		2	168.6541	12.8182	0.00211	7.42	-22.35	9.0	C	9.0	73.9	
NGC4278		1	185.0284	29.2808	0.00206	7.18	-23.84	16.0		16.0	237.3	
NGC4438		2	186.9403	13.0088	0.00035	7.27	-23.06	11.6	C	11.6	135.3	
NGC4486	M 87	1	187.7059	12.3911	0.00420	5.81	-25.34	17.0	C	17.0	323.0	
NGC4694		1	192.0629	10.9836	0.00388	8.96	-22.06	16.0		16.0	55.5	
UGC3426	Mrk 3	1	93.9012	71.0375	0.01300	8.97	-24.75	55.0		55.5	244.6	

Notes:

- 1 Galaxy identifier
- 2 Alternative identifier.
- 3 Catalog: 1 - B11, 2 - extended, 3 - supplementary.
- 4,5,6 RA, Dec and redshift z from are from SIMBAD.
- 7,8 m_K from the 2MASS catalog (Skrutskie et al. 2006), M_K calculated from the luminosity distance.
- 9 Distance (Mpc) from COSMICFLOWS-3 or NED, as described in the text.
- 10 C - source of distance information from COSMICFLOWS-3.
- 11 Luminosity distance calculated from TOPCAT functionality.
- 11 Stellar velocity dispersion in km s^{-1} .
- 12 Velocity dispersion source; no flag - HyperLeda, S - SDSS spectra.

Table 7b. Sample of the catalog of “Radio Active” galaxies, extending the B11 catalog - Part 2. (The full table is available online)

Galaxy (1)	T Type (14)	Activity (15)	Mod. (16)	$\log M_\bullet$ (17)	Ref (18)	Flux (19)	e_Flux (20)	Ref (21)	UL (22)	$\log P$ (23)	Obs (24)	Surveys (25)
2MASX J16251687-0910524	-1			9.14	K	4.6	0.5			21.90	*	17
IC0450	-0.5	Sy1.5		9.00	K	269.5	8.1			23.29	*	14
IC5063	-0.8	Sy1		7.54		1975.0	59.3	S		23.71		12 14 17
NGC0080	-2.5			8.76		0.9	0.5		<	20.89		
NGC0447	0			7.63		6.0	4.0	A	<	21.65		3
NGC1052	-5	LIN		8.76		1100.0	100.0			22.68	*	7 10 11 12
NGC1316	-2	AGN		8.49		150000.0	10000.0			24.90		10
NGC2217	-1	LIN		8.41		22.0	1.0			21.24		10 12
NGC3182	1	Sy2		6.80		2.3	0.5			20.37	*	1 3 13 17
NGC3593	0	Sy2	*	5.75		86.2	3.4			20.92	*	8 13 17
NGC4278	-5	LIN		9.15		390.0	10.0			22.08	*	11 13
NGC4438	0	LIN		7.25		63.3	2.7			21.01	*	11
NGC4486	-4	LIN		10.04		210000.0	10000.0			24.86		1 11 13
NGC4694	-2	HII		5.04		3.5	0.5			20.03	*	1 13 16
UGC3426	-2	Sy1		8.72		1100.0	100.0			23.61	*	

Notes:

- 1 Galaxy identifier
- 14 Morphological type from de Vaucouleurs et al. (1991).
- 15 Nuclear activity type, consolidated from (Véron-Cetty & Véron 2006), SIMBAD or NED.
- 16 Activity type modified, * - re-measured from NED spectra (see text).
- 17 Black hole mass (units of $\log M_\odot$), computed as described in text.
- 18 M_\bullet source, K - computed from M_K , otherwise from σ .
- 19,20 Radio flux and uncertainty (mJ).
- 21 Radio flux reference. blank - NVSS, F - VLA FIRST, A - Arecibo, S - SUMSS, P - Parkes-MIT-NRAO, W- Whiteoak.
- 22 Radio upper limit flag.
- 23 Log radio power (W Hz^{-1}).
- 24 Observed. * - observed with TripleSpec.
- 25 Surveys. As described in the main text and listed in Table 8.

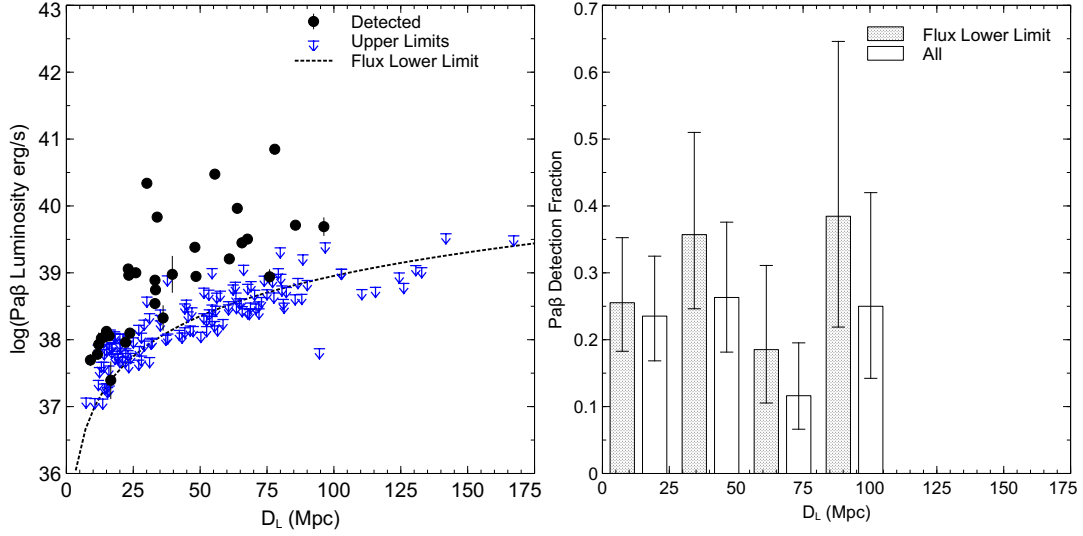


Figure 11. Left panel: Pa β log luminosities and upper limits vs. luminosity distance. The flux lower limit of 7.5×10^{-16} erg cm $^{-2}$ s $^{-1}$ is plotted. Right panel: Histogram of Pa β detection fraction vs. luminosity distance bin, showing fraction for all objects and for those above the flux lower limit. No bias of detection rates with luminosity distance is apparent.

Table 8. Spectral and IFU surveys, for Table 7

ID	Survey	#	Reference
1	ATLAS3D-SAURON	36	Cappellari et al. (2011)
2	SAMI	2	Scott et al. (2018)
3	CALIFA	2	Sánchez et al. (2012)
4	SDSS MANGA	2	Abdurro’uf et al. (2022)
5	KONA	1	Müller-Sánchez et al. (2018)
6	LLAMA	1	Lin et al. (2018)
7	AGN-IFS	3	Storchi-Bergmann (2013)
8	NUGA	4	García-Burillo et al. (2007)
9	GATOS	1	García-Burillo et al. (2021)
10	DIVING3D	44	Steiner et al. (2022)
11	PALOMAR	21	Filippenko & Sargent (1985)
12	6dFGS	246	Jones et al. (2004, 2009)
13	SDSS Spectra	77	Abdurro’uf et al. (2022)
14	BASS	22	Koss et al. (2022)
15	GAMA	7	Driver et al. (2009)
16	PHANGS	6	Leroy et al. (2021)
17	AllskyAGN	76	Zaw et al. (2019)

measured the emission line fluxes for H, He, [Fe II] and H $_2$ and determined the nuclear excitation mechanisms, noting a population which are optically classified as star-forming, but have AGN emission line ratios in the infrared, most likely due to the better dust penetration in the infrared.

By stacking spectra showing H $_2$ emission, we deduced the H $_2$ excitation temperature (1957 ± 182 K) and dominant excitation mechanism (thermal and shock heating combined) from the K -band emission line sequence. When binned by low or high power radio emission, the lower power bin is warmer than the higher power. This may be explained by the relative balance of heating mechanisms changing at higher radio power.

By stacking those spectra that have no emission lines, we have produced an “average” spectrum of the continuum, showing the main absorption features and the proposed spectral indices from the literature. Plotting the CO12 absorption line index vs. $J - K$ colour shows a trend, with stronger nuclear activity producing a weaker CO12 index and a redder (flatter) continuum.

We have explored the correlations between the radio and various emission-line luminosities; finding a trend with radio power for all NIR emission lines. However, we deduced from the large scatter in the upper limits to NIR emission lines that the two are not directly coupled and that the duty cycles of SF and AGN activity are not synchronised.

We have also presented the complete early-type radio galaxy catalog, where the original published in B11, which focused on elliptical and S0 galaxies, has been supplemented with S0/a plus some later type galaxies, with supplementary objects that were observed in the NIR with Triplespec, making a total of 546 objects. This catalog contains K band magnitudes, stellar dispersions, distances, black hole mass estimates and radio flux and power, as well as morphology and activity information.

ACKNOWLEDGEMENTS

We would like to thank our Triplespec colleagues at Caltech for their support of our survey; thanks go to Eilat Glickman for sharing her observing expertise at the Palomar 200” telescope and her copy of the Triplespec SpexTool IDL program. The Caltech-Swinburne Collaborative Agreement allowed JM access to the Hale telescope. This research has made use of the NASA/IPAC Extragalactic Database (NED) which is operated by the Jet Propulsion Laboratory, California Institute of Technology, under contract with the National Aeronautics and Space Administration. This publication makes use of data products from the Two Micron All Sky Survey, which is a joint project of the University of Massachusetts and the Infrared Processing and Analysis Center/Caltech, funded by NASA and the U.S. National Science Foundation. This research has also made use of the SIMBAD database, operated at CDS, Strasbourg, France (Wenger et al. 2000).

This paper makes use of SDSS data. Funding for the Sloan Digital Sky Survey IV has been provided by the Alfred P. Sloan Foundation, the U.S. Department of Energy Office of Science, and the Participating Institutions. SDSS acknowledges support and re-

sources from the Center for High-Performance Computing at the University of Utah. The SDSS web site is www.sdss.org.

SDSS is managed by the Astrophysical Research Consortium for the Participating Institutions of the SDSS Collaboration including the Brazilian Participation Group, the Carnegie Institution for Science, Carnegie Mellon University, Center for Astrophysics, Harvard & Smithsonian (CfA), the Chilean Participation Group, the French Participation Group, Instituto de Astrofísica de Canarias, The Johns Hopkins University, Kavli Institute for the Physics and Mathematics of the Universe (IPMU) / University of Tokyo, the Korean Participation Group, Lawrence Berkeley National Laboratory, Leibniz Institut für Astrophysik Potsdam (AIP), Max-Planck-Institut für Astronomie (MPIA Heidelberg), Max-Planck-Institut für Astrophysik (MPA Garching), Max-Planck-Institut für Extraterrestrische Physik (MPE), National Astronomical Observatories of China, New Mexico State University, New York University, University of Notre Dame, Observatório Nacional / MCTI, The Ohio State University, Pennsylvania State University, Shanghai Astronomical Observatory, United Kingdom Participation Group, Universidad Nacional Autónoma de México, University of Arizona, University of Colorado Boulder, University of Oxford, University of Portsmouth, University of Utah, University of Virginia, University of Washington, University of Wisconsin, Vanderbilt University, and Yale University.

Facilities: Tripplespec on Palomar 200''

DATA AVAILABILITY

Tables 2, 3, 7 and 8 plus the reduced, restframe spectra are available in full at CDS via anonymous ftp to [cdsarc.u-strasbg.fr](ftp://cdsarc.u-strasbg.fr) (130.79.128.5) or via <https://cdsarc.unistra.fr/viz-bin/cat/J/MNRAS/????/???>.

REFERENCES

- Abdurro'uf et al., 2022, *ApJSS*, 259, 35
 Baldwin J. A., Phillips M. M., Terlevich R., 1981, *PASP*, 93, 5
 Becker R. H., White R. L., Helfand D. J., 1995, *ApJ*, 450, 559
 Black J. H., van Dishoeck E. F., 1987, *ApJ*, 322, 412
 Brown M. J. I., Jannuzi B. T., Floyd D. J. E., Mould J. R., 2011, *ApJ*, 731, L41
 Brown M. J. I., et al., 2017, *ApJ*, 847, 136
 Busch G., Eckart A., Valencia-S. M., Fazeli N., Scharwächter J., Combes F., García-Burillo S., 2017, *A&A*, 598, A55
 Capetti A., et al., 2022, *A&A*, 660, A93
 Cappellari M., et al., 2011, *MNRAS*, 413, 813
 Cardelli J. A., Clayton G. C., Mathis J. S., 1989, *ApJ*, 345, 245
 Cesetti M., et al., 2009, *A&A*, 497, 41
 Cesetti M., Pizzella A., Ivanov V. D., Morelli L., Corsini E. M., Dalla Bontà E., 2013, *A&A*, 549, 1
 Condon J. J., Cotton W. D., Greisen E. W., Yin Q. F., Perley R. A., Taylor G. B., Broderick J. J., 1998, *AJ*, 115, 1693
 Cushing M. C., Vacca W. D., Rayner J. T., 2004, *PASP*, 116, 362
 Cutri R. M., Rieke G. H., Lebofsky M. J., 1984, *ApJ*, 287, 566
 Davies R. I., Sternberg a., Lehnert M., Tacconi-Garman L. E., 2003, *ApJ*, 597, 907
 Davies R. I., Sternberg A., Lehnert M. D., Tacconi-Garman L. E., 2005, *ApJ*, 633, 105
 Davies R. I., Mueller Sanchez F., Genzel R., Tacconi L. J., Hicks E. K. S., Friedrich S., Sternberg A., 2007, *ApJ*, 671, 1388
 Davies R. I., et al., 2009, *Proc. Int. Astron. Union*, 5, 283
 Dors Jr O. L., Riffel R. A., Cardaci M. V., Hägele G. F., Krabbe A. C., Pérez-Montero E., Rodrigues I., 2012, *MNRAS*, 422, 252
 Draine B. T., Woods D. T., 1990, *ApJ*, 363, 464
 Dressel L. L., Condon J. J., 1978, *ApJSS*, 36, 53
 Driver S. P., Norberg P., Baldry I. K., Bamford S. P., Hopkins A. M., Liske J., Loveday J., Peacock J. A., 2009, *Astron. Geophys.*, 50, 5.12
 Durré M., Mould J., 2018, *ApJ*, 867, 149
 Filippenko A. V., Sargent W. L. W., 1985, *ApJSS*, 57, 503
 García-Burillo S., Combes F., Usero A., Graciá-Carpio J., 2007, *New Astron. Rev.*, 51, 160
 García-Burillo S., et al., 2021, *A&A*, 652, A98
 Gasparri D., et al., 2021, *MNRAS*, 507, 4669
 Gehrels N., 1986, *ApJ*, 303, 336
 Graham A. W., Scott N., 2013, *ApJ*, 764, 151
 Gregory P. C., Vavasour J. D., Scott W. K., Condon J. J., 1994, *ApJSS*, 90, 173
 Herter T. L., et al., 2008, *Proc. SPIE*, 7014, 70140X
 Hollenbach D., McKee C. F., 1989, *ApJ*, 342, 306
 Hubbard E. N., Puetter R. C., 1985, *ApJ*, 290, 394
 Hummer D. G., Storey P. J., 1987, *MNRAS*, 224, 801
 Jones D. H., et al., 2004, *MNRAS*, 355, 747
 Jones D. H., et al., 2009, *MNRAS*, 399, 683
 Kennicutt R. C. J., 1998, *Annu. Rev. Astron. Astrophys.*, 36, 189
 Kennicutt R. C., et al., 2009, *ApJ*, 703, 1672
 Kewley L. J., Groves B., Kauffmann G., Heckman T., 2006, *MNRAS*, 372, 961
 Koss M. J., et al., 2022, *ApJSS*, 261, 1
 Krabbe A., Sams III B., Genzel R., Thatte N., Prada F., 2000, *A&A*, 354, 439
 Kwan J., 1977, *ApJ*, 216, 713
 Larkin J. E., Armus L., Knop R. A., Soifer B. T., Matthews K., 1998, *ApJSS*, 114, 59
 Leitherer C., et al., 1999, *ApJSS*, 123, 3
 Leroy A. K., et al., 2021, *ApJSS*, 257, 43
 Lin M.-Y., et al., 2018, *MNRAS*, 473, 4582
 Makarov D., Prugniel P., Terekhova N., Courtois H., Vauglin I., 2014, *A&A*, 570, A13
 Maloney P. R., Hollenbach D. J., Tielens A. G. G. M., 1996, *ApJ*, 466, 561
 Martins L. P., Rodríguez-Ardila A., Diniz S., Gruenwald R., de Souza R., 2013, *MNRAS*, 431, 1823
 Mason R. E., et al., 2015, *ApJSS*, 217, 13
 Mauch T., Murphy T., Buttery H. J., Curran J., Hunstead R. W., Piestrzynski B., Robertson J. G., Sadler E. M., 2003, *MNRAS*, 342, 1117
 McAlary C. W., Rieke G. H., Lebofsky M. J., Stocke J. T., 1986, *ApJ*, 301, 105
 Meyer M. R., Edwards S., Hinkle K. H., Strom S. E., 1998, *ApJ*, 508, 397
 Morelli L., et al., 2020, *A&A*, 641, A44
 Mould J., et al., 2012, *ApJSS*, 203, 14
 Mouri H., 1994, *ApJ*, 427, 777
 Müller-Sánchez F., Hicks E. K. S., Malkan M., Davies R., Yu P. C., Shaver S., Davis B., 2018, *ApJ*, 858, 48
 Ogle P., Boulanger F., Guillard P., Evans D. A., Antonucci R., Appleton P. N., Nesvadba N., Leipski C., 2010, *ApJ*, 724, 1193
 Ott T., 2012, QFitsView: FITS file viewer, Astrophysics Source Code Library:1210.019, <https://ascl.net/1210.019>
 Quillen A. C., Alonso-Herrero A., Rieke M. J., Rieke G. H., Ruiz M., Kulkarni V., 1999, *ApJ*, 527, 696
 Rayner J. T., Cushing M. C., Vacca W. D., 2009, *ApJSS*, 185, 289
 Reunanen J., Kotilainen J. K., Prieto M. A., 2002, *MNRAS*, 331, 154
 Ricci F., et al., 2022, *ApJSS*, 261, 8
 Riffel R. A., Storch-Bergmann T., 2011, *MNRAS*, 417, 2752
 Riffel R. A., Storch-Bergmann T., Winge C., McGregor P. J., Beck T., Schmitt H., 2008, *MNRAS*, 385, 1129
 Riffel R., Pastoriza M. G., Rodríguez-Ardila A., Bonatto C., 2009, *MNRAS*, 400, 273
 Riffel R. A., Storch-Bergmann T., Nagar N. M., 2010, *MNRAS*, 404, 166
 Riffel R., Rodríguez-Ardila A., Aleman I., Brotherton M. S., Pastoriza M. G., Bonatto C., Dors O. L., 2013, *MNRAS*, 430, 2002
 Riffel R. A., Vale T. B., Storch-Bergmann T., McGregor P. J., 2014, *MNRAS*, 442, 656

- Riffel R. A., Storchi-Bergmann T., Riffel R., 2015, *MNRAS*, 451, 3587
- Riffel R. A., Storchi-Bergmann T., Riffel R., Dahmer-Hahn L. G., Diniz M. R., Schönell A. J., Dametto N. Z., 2017, *MNRAS*, 470, 992
- Riffel R., et al., 2019, *MNRAS*, 486, 3228
- Riffel R. A., Bianchin M., Riffel R., Storchi-Bergmann T., Schönell A. J., Dahmer-Hahn L. G., Dametto N. Z., Diniz M. R., 2021a, *MNRAS*, 503, 5161
- Riffel R. A., et al., 2021b, *MNRAS*, 504, 3265
- Rodriguez-Ardila A., Riffel R., Pastoriza M. G., 2005, *MNRAS*, 364, 1041
- Roueff E., Abgrall H., Czachorowski P., Pachucki K., Puchalski M., Komasa J., 2019, *A&A*, 630, A58
- Sabater J., et al., 2019, *A&A*, 622, A17
- Sahu N., Graham A. W., Davis B. L., 2019, *ApJ*, 887, 10
- Sánchez S. F., et al., 2012, *A&A*, 538, A8
- Schartmann M., Mould J., Wada K., Burkert A., Durré M., Behrendt M., Davies R. I., Burtscher L., 2017, *MNRAS*, 473, 953
- Schlafly E. F., Finkbeiner D. P., 2011, *ApJ*, 737, 103
- Schönell A. J., Storchi-Bergmann T., Riffel R. A., Riffel R., 2017, *MNRAS*, 464, 1771
- Scott N., et al., 2018, *MNRAS*, 481, 2299
- Skrutskie M. F., et al., 2006, *AJ*, 131, 1163
- Smee S. A., et al., 2013, *AJ*, 146, 32
- Smith D., 1995, *A&A*, 296, 789
- Steiner J. E., et al., 2022, *MNRAS*, 510, 5780
- Sternberg A., Dalgarno A., 1989, *ApJ*, 338, 197
- Storchi-Bergmann T., 2013, *Proc. Int. Astron. Union*, 9, 354
- Storchi-Bergmann T., McGregor P. J., Riffel R. A., Simões Lopes R., Beck T., Dopita M., 2009, *MNRAS*, 394, 1148
- Taylor M. B., 2005, TOPCAT & STIL: Starlink Table / VOTable Processing Software, <https://ascl.net/1101.010>
- Tully R. B., Courtois H. M., Sorce J. G., 2016, *AJ*, 152, 50
- Véron-Cetty M.-P., Véron P., 2006, *A&A*, 455, 773
- Wallace L., Meyer M. R., Hinkle K., Edwards S., 2000, *ApJ*, 535, 325
- Wenger M., et al., 2000, *Astron. Astrophys. Suppl. Ser.*, 143, 9
- Whiteoak J., 1970, *Astrophys. Lett.*, 5, 29
- Wilman R. J., Edge A. C., Johnstone R. M., 2005, *MNRAS*, 359, 755
- Zaw I., Chen Y.-P., Farrar G. R., 2019, *ApJ*, 872, 134
- Zubovas K., King A., 2019, *MNRAS*, 484, 1829
- Zubovas K., Nayakshin S., King A., Wilkinson M., 2013, *MNRAS*, 433, 3079
- de Vaucouleurs G., de Vaucouleurs A., Corwin H. G. J., Buta R. J., Paturel G., Fouqué P., 1991, Third Reference Catalogue of Bright Galaxies. Springer-Verlag, New York, <http://vizier.u-strasbg.fr/viz-bin/VizieR?-source=VII/155>

This paper has been typeset from a $\text{\TeX}/\text{\LaTeX}$ file prepared by the author.